Assessing errors in optical properties due to particle asphericity and inhomogeneity

A. Smith, R. Grainger, G. Thomas, E. Carboni

Atmospheric, Oceanic and Planetary Physics
Department of Physics
University of Oxford

February 2009

4.1.2 Assessing errors in optical properties due to particle asphericity and inhomogeneity

In order to quantify the error in non-spherical aerosol optical properties a method proposed by Dubovik (2006) will be followed. In this method the computation time is reduced for the calculation of light scattering by a mixture of spheroids by parameterizing the numerical integration of spheroid optical properties over size and shape using look-up tables of quadrature coefficients. These coefficients will be determined using existing T-matrix code for sand, ash, salt, ammonium sulphate and ammonium nitrate and black carbon aerosol.

Depending on humidity, water condenses on the non-soluble particles to form spherical particles. These cases will be modelled using Mie code for layered spheres (Bohren & Huffman, 1998).

Optical properties (single scatter albedo, extinction coefficient and phase function) produced by this method will then be compared to equivalent properties produced using Mie scattering alone, thus providing a quantitative measure of the improvement. These studies complement the laboratory work to be completed within CP3 and could link into the scattering and radiative transfer model framework to be initiated within that activity.

Contents

Chapter 1

Introduction

The assumption of particle sphericity has long been a standard part of any aerosol retrieval algorithm. While, for particles small relative to the scattering light's wavelength, this may be a safe approach (being in the Rayleigh regime), it well known that spheres are not a good representation of the scattering aerosol typically found in the atmophere [Koepke and Hess, 1988]. Commonly found shapes can be agglomorate particles (such as the by-products of biomass burning), large irregular mineral dust particles (such as sand), crystalised salts or particles with liquid coatings [Colbeck, 1998], all of which are clearly either nonspherical or inhomogeneous (or both).

Convinced that the aerosol are not homogeneous spheres, a problem arises. The assumption of sphericity brings huge simplicity to light scattering calculations, due in large part to the symmetry of the problem. If we are to use this assumption, are the errors resulting from it managable? Are there alternative methods which can more accurately model the shape, without adding unmanageable computational complexity? This is the subject of the following report.

Various standard types of aerosol will be discussed, paying attention to the different assumptions about their shape and structure which can be made. This will be compared to the spherical models usually employed. The two non-spherical (NS) methods used are to apply coatings to spheres (to make non-homogeneous spheres) and the T-matrix method which can in principle be used to model the light scattering properties of particles of any shape. The following T-matrix calculations will use only spheroidal particle shapes (ellipses which have been rotated about either their minor or major axis. As a result, these are rotationally symmetric, reducing the complexity of computation by many orders of magnitude.

Comparisons will also be made with the aerosol section of the **O**xford-**R**AL retrieval of **A**erosol and **C**loud algorithm (ORAC). Specifically, the desert dust class will be investigated. Test retrievals of known sand filled satellite images will be compared to new retrievals with updated optical properties, no longer based on spherical light scatterers.

1.1 Aerosol properties

For a sample of spherical, atmospheric aerosol, only a small number of parameters are required to fully describe it's optical properties. Firstly, we assume that the particles are homogeneous, and have a known refractive index (RI). Secondly, assuming the number distribution of sizes, $n(r)$, is lognormal, the median radius, r_g, and σ (the standard deviation of $\ln r$) are all that is required to fully compute the ensemble's light scattering properties. The lognormal distribution is defined in

this case as:

$$n(r) = \frac{1}{\sigma\, r\, \sqrt{2\pi}}\, \exp\left[-\frac{1}{2}\left(\frac{\ln r - \ln r_g}{\sigma}\right)^2\right]. \tag{1.1}$$

The refractive index is then used, along with Mie theory to calculate the light interaction properties of the aerosol. In this report, refractive index values and distribution properties of the various aerosol types are obtained using data, for the most part, from the **O**ptical **P**roperties of **A**erosols and **C**louds software package (OPAC) [Hess et al., 1998], but also from a study of Dubovik et al. [2002].

As soon as we remove our assumption of spherical, homogeneous particles, additional aerosol properties begin to appear. Most analysis of particle shape is only partially quantitive in that a sample of particulate is generally inspected under an electron microscope, and the shape properties of these few are manually measured. As such, we are only looking at a two dimensional image of the aerosol, and various parameters are used to characterise shape.

Aspect ratio (AR) The first is the AR, defined as the ratio of length along maximum projection of the shape and the width (perpendicular to that projection). This is very similar to the parameter ϵ given in definition of spherioids and gives the ratio of a/b for the two independant axes of the ellipse which is to be rotated. For $\epsilon = 1$ we have a sphere; $\epsilon < 1$ implies a prolate spheroid (e.g. rugby ball); $\epsilon > 1$ implies an oblate spheroid (e.g. a disk).

Circularity (CIR) Second, the CIR gives a measure of how a particle's projected perimeter compares to its projected area. It is usually defined as $CIR = \text{perimeter}^2/(4\pi A)$ (e.g. Kalashnikova and Sokolik [2004]) or the reciprocal of this expression. In some literature, it is called the shape factor, Sh. As with AR, CIR should be unity for a perfect sphere.

Fractal dimension When looking at aggregate particles (such as fresh products of combustion), it is often true that their shapes are scale invariant [Sorensen, 2001]. In this case, a fractal dimension is a useful quantity. Essentially, a very similar quantity to circularity, it tells us how a agglomerate particle's length relates to its mass. e.g. In Wentzel et al. [2003], they define it as D_f in the equation $N_p \propto \left(\frac{R_g}{r_p}\right)^{D_f}$, where R_g is some radius of a particle describing overall size, and r_p is the radius of an individual spherule within the whole.

There are also measurement parameters which take account of non-sphericity in three dimensions, such as the dynamic shape factor given by Kaaden et al. [2008]. Since these generally don't provide information about specific shape (so much as about the correction required to the spherical case), they are not particularly useful in this case.

Refractive index values

As a brief aside, one should be careful about the method used to obtain an aerosols refractive index. If the method involves assuming the shape of the particle (almost certainly as a sphere), attempting later to model this particle using Mie theory may be more successful than if the correct refractive index (but wrong scattering method) is used.

List of current assumptions

As an example, the ORAC retrieval currently makes the following assumptions about the aerosol classes it is retrieving.

- All aerosols are spherical.
- All aerosols are homogeneous.
- No particles have coatings or inclusions.
- Soluble particles form spherical solution droplets in humid conditions. Furthermore, humidity is fixed at 50%, so this is always the case.
- Insoluble particles are not affected by humidity (e.g. by being coated).
- None of the aerosol components have rough surfaces or form aggregates with nearby particles.

1.2 Optical properties

Phase function

The phase function is a normalised measure of how the intensity of scattered light varies with scattering angle. For a single, spherical particle, with unpolarised light, it is defined as [van de Hulst, 1957, Bohren and Huffman, 1983]:

$$P(\theta) = \frac{2}{C_{\text{sca}}\, k^2\, r^2} \left(|S_1(\theta)|^2 + |S_2(\theta)|^2 \right), \tag{1.2}$$

where C_{sca} is the scattering cross-section and S_1 and S_2 are the amplitude functions for perpendular and parallel components of the electric field. If we know the incident irradiance, I_0, the scattered intensity can be calculated as

$$I = I_0\, C_{\text{sca}} P(\theta). \tag{1.3}$$

Extinction and scattering cross sections

Cross-sections tell us how much of an incident beam's intensity is taken away in terms of the area of the beam[1]. If the power taken away by a certain process is W_x, then the cross-section for this process, C_x, is:

$$C_x = \frac{W_x}{\frac{1}{2}\sqrt{\frac{\epsilon}{\mu}}|\mathbf{E}_{i\,0}|^2},$$

where ϵ and μ are the permitivity and permiability respectively. The incident electric field is $\mathbf{E}_{i\,0}$.

For example, the scattering cross-section, C_{sca} tells us what area of the incident beam becomes scattered light. The extinction cross-section, C_{ext}, tells us how much of the incident light is removed from the incident beam by scattering and absorption.

Single scattering albedo

The single scattering albedo tells us the probablilty that a light interacting with a volume will be scattered (the other option being that it is absorbed). As such, it can be defined as

$$\text{SSA} \ = \bar{\omega_0} = \frac{C_{\text{sca}}}{C_{\text{ext}}} \tag{1.4}$$

The range of values is $0 \leq \bar{\omega_0} \leq 1$.

[1] The cross section is taken in a plane perpendicular to the direction of the incident beam.

1.3 Scattering methods

Mie theory

Mie theory was developed by Gustav Mie in 1908 in order to understand the colours that resulted from light scattering from gold particles suspended in water. Although it is exact, only with the emergence of computing has it become practical to calculate the scattering values. An excellent introduction to the theory is provided in Bohren and Huffman [1983], whose notation and outline I have used. Code to calculate Mie scattering in the IDL programming language can be found on the AOPP, Oxford website[2].

An incident, electromagnetic, x-polarised plane wave is expressed in vector spherical wave functions (VSWF) , $\mathbf{M}_{mn}(k\mathbf{r})$ and $\mathbf{N}_{mn}(kr,\theta,\phi)$, which are solutions to $\nabla^2\mathbf{E}+k^2\mathbf{E}=0$, in spherical coordinates. The incident electric field is shown to be

$$\mathbf{E}_i = E_0\sum_{n=1}^{\infty} i^n \frac{2n+1}{n(n+1)}\left(\mathbf{M}_{o1n}^{(1)} - i\mathbf{N}_{e1n}^{(1)}\right), \tag{1.5}$$

and the magnetic field can then be simply obtained from $\nabla\times\mathbf{H} = -i\omega\epsilon\mathbf{E}$ where ϵ is the electric permittivity and ω the frequency. Applying boundary conditions at the sphere radius, r_0,

$$(\mathbf{E}_i+\mathbf{E}_s-\mathbf{E}_I)\times\hat{\mathbf{e}}_r = (\mathbf{H}_i+\mathbf{H}_s-\mathbf{H}_I)\times\hat{\mathbf{e}}_r = 0 \qquad (\text{for } r=r_0), \tag{1.6}$$

and writing the scattered field, $\mathbf{E}_s$ and internal field, $\mathbf{E}_I$, as a similar sum of VSWFs to our incident field, we find our scattered field solution, which turns out to be a sum of Riccati-Bessel functions and associated Legendre functions.

Coated spheres

For coated spheres, we only need to extend the theory of the previous section. Boundary conditions are imposed at the boundary between 1st and 2nd media as well as between the 2nd media and the containing medium. After these are satisfied, we have a very similar solution to the Mie case. Details of this can be found in Bohren and Huffman [1983], pp181–183.

T-matrix method

The main method used in the following work is the T-matrix method. This writes the incident field as a sum of VSWFs,

$$\mathbf{E}_i(\mathbf{r}) = \sum_{n=1}^{\infty}\sum_{m=-n}^{n}\left[a_{mn}\,\mathbf{M}_{mn}^{(1)}(k\mathbf{r}) + b_{mn}\,\mathbf{N}_{mn}^{(1)}(k\mathbf{r})\right], \tag{1.7}$$

the scattered field similarly,

$$\mathbf{E}_s(\mathbf{r}) = \sum_{n=1}^{\infty}\sum_{m=-n}^{n}\left[p_{mn}\,\mathbf{M}_{mn}^{(3)}(k\mathbf{r}) + q_{mn}\,\mathbf{N}_{mn}^{(3)}(k\mathbf{r})\right], \tag{1.8}$$

and the field on the surface of the scattering object as

$$\hat{\mathbf{n}}\times\mathbf{E}(mk\mathbf{r}) = \hat{\mathbf{n}}\times\sum_{n=1}^{\infty}\sum_{m=-n}^{n}\left[c_{mn}\,\mathbf{M}_{mn}^{(1)}(mk\mathbf{r}) + d_{mn}\,\mathbf{N}_{mn}^{(1)}(mk\mathbf{r})\right], \tag{1.9}$$

[2] `http://www-atm.physics.ox.ac.uk/code/mie/` Details of the code are given in Grainger et al. [2004].

where m is the refractive index and bracketed superscripts on the VSWFs denote specific solutions [Mishchenko et al., 2000], one can use the orthogonality properties of VSWFs to obtain relationships between *just* a_{mn} and b_{mn} or *just* p_{mn} and q_{mn} and the surface fields on our scattering object. These relationships can be written:

$$\begin{bmatrix}\mathbf{a}\\ \mathbf{b}\end{bmatrix} = \mathbf{Q_1}\begin{bmatrix}\mathbf{c}\\ \mathbf{d}\end{bmatrix}, \qquad \begin{bmatrix}\mathbf{p}\\ \mathbf{q}\end{bmatrix} = \mathbf{Q_2}\begin{bmatrix}\mathbf{c}\\ \mathbf{d}\end{bmatrix}, \tag{1.10}$$

and so we can relate the unknown scattering coefficients ($\mathbf{p}$, $\mathbf{q}$), to the known incident field coefficients ($\mathbf{a}$, $\mathbf{b}$) by

$$\begin{bmatrix}\mathbf{p}\\ \mathbf{q}\end{bmatrix} = \mathbf{Q_2}\mathbf{Q_1^{-1}}\begin{bmatrix}\mathbf{a}\\ \mathbf{b}\end{bmatrix}, \tag{1.11}$$

where the T-matrix, $\mathbf{T} = \mathbf{Q_2}\mathbf{Q_1^{-1}}$. The matrices $\mathbf{Q_1}$ and $\mathbf{Q_2}$ are to be found, from which the scattered field can be easily calculated.

1.3.1 Additional modeling methods

The discrete dipole approximation (DDA) can in theory calculate the light scattering characteristics of almost any shape, at the price of much greater computational complexity. It also suffers from the disadvantage (not present in T-matrix or layered sphere methods) that for each incoming and outgoing light direction incident on the particle, the entire calculation must be repeated. In contrast, techniques which solve the wave equation as an expansion of vector spherical wave functions (VSWF) such as Mie theory or the T-matrix method, do not need to recalculate when reorientating their particles. In a system such as the atmosphere, where a hugh distribution of randomly orientated particles are involved, this problem make DDA cumbersome.

A second group of methods concentrate on aggregate particles. There are basically two ways to proceed. One can look at individual particles, with a specific build up of spheres which represent a shape such as that shown in Fig. 2.7. These scattering solutions can be calculated exactly, although they are time consuming[Xu and Gustafson, No date]. Aggregates can also be modelled as a statistical ensemble of fractal particles with a fractal dimension, D [Sorensen, 2001].

1.4 Measuring methods

Measurement of particles by their light scattering properties can most generally be split into two techniques. Firstly, individual particles can be investigated using illumination (generally by a laser beam), and a portion of their phase function measured. An advantage is that we can measure a large part of the phase function if we put our minds to it, and thus hopefully constrain our particles properties more tightly. However, individual particle measurements are likely to be strongly affected by nonsphericity since orientation and shape (as well as size and refractive index) will alter the measured phase function.

The second method involved looking at the light scattered by a distribution of particles in the atmosphere using either the sun (satellite observations, AERONET stations) or a laser (LIDAR measurements). Depending on the geometry of the experiment, various parts of the phase function would be measured. Nadir viewing instruments generally measure backscattered light, for example, as do instruments on geostationary platforms and LIDAR instruments. Occulation instruments measure forward scatter. When multiple particles are being measured, the phase function is invariably

"blurred" by the wide variety of sizes of particle investigated. Further "smoothing" of the phase function is caused by the inclusion of NS particles.

Chapter 2

Aerosol types

In this chapter, aerosol characteristics will be described, and suitable alternative calculations to spherical calculations will be shown.

2.1 Sea salt

2.1.1 Background

Salt aerosol particles, being hygroscopic, can usually be modeled as spheres [Chamaillard et al., 2006]. Especially in maritime environments, the humidity of the air can make this a valid asumption, but in dry conditions, agglomerates or cubic particles can be found (e.g. Fig. 2.1a). To further complicate the problem, the shape of salt with respect to relative humidity (RH) follows a hysteresis curve [Lewis and Schwartz, 2004]. When the RH increases, a single dry salt particle has no change in size until a critical RH at which point there is a phase transition to a saturated solution. This transition is known as deliquescence. If the solution then finds the RH decreasing, evaporation occurs up until the point of saturation. Then, the particles size stays fixed with decreasing RH, and the drop is supersaturated until a point at which there is a phase transition back to a dry particle known as efflorescence. This is shown in Fig. 2.1b.

Thus we have two regimes, with two different potential pitfalls. For dry salt, the shape will be angular and crystaline. For liquid solutions of salt, we have spherical particles, but the RI will vary with the concentration of salt in the solution. Additionally, we cannot use instantaneous humidity values as an indication of what phase the particles will be in, since the hysteresis curve means that the phase is determined by the history of the particle.

With mean particle sizes of 1.9 μm in the midtroposphere [Gong et al., 2002], the larger dry particles will definitely be in the regime where they could alter phase functions significantly. However, the more pressing concern is that of refractive index.

2.1.2 Optical calculations

Using the OPAC aerosol data, there is a striking difference in the real part of refractive index for the dry aerosol. This is hardly surprising, since we are changing from a solid, to a solution of ions. This will have a far greater impact on the phase function, and other optical measurements, than will the secondary effects of non-sphericity (for which one still requires the refractive index). As such, in this case, instead of looking at NS particles, we look at how the varying humidity affects the optical properties.

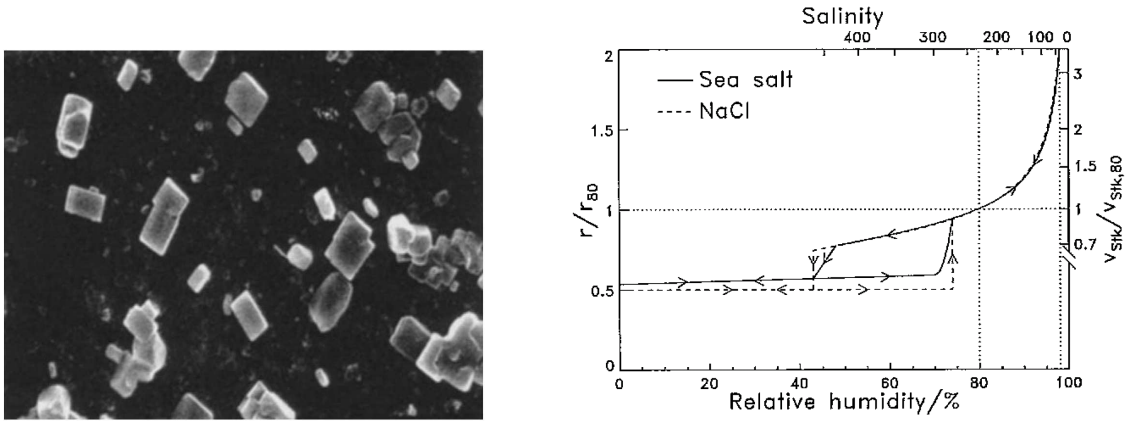

(a) (b)

Figure 2.1: Sea salt characteristics: a) SEM image of dried sea salt from the west coast of Ireland. From Chamaillard et al. [2006]. b) Dependence of sea salt's equilibrium radii on relative humidity. Reproduced from Lewis and Schwartz [2004].

Fig. 2.2 shows the phase function for three cases: Dry sea salt, 50 % relative humidity, and 99 % RH. Refractive indices are provided with the figure. In the ORAC retrieval, it is assumed that for all water soluble aerosol, the relative humidity is 50 %. Because of this, differences between the other particle values are compared to this.

Particularly for the dry particles, there is are significant changes in the phase function (up to 200% differences in the backscatter). As water has more of an effect in the scattering, with increasing RH, we see the backscatter peaks move forward. There is very low aborption, so single scatter albedo is high. The scattering cross section is not hugely effected by the change in humidity.

NONSPHERICAL CALCULATIONS

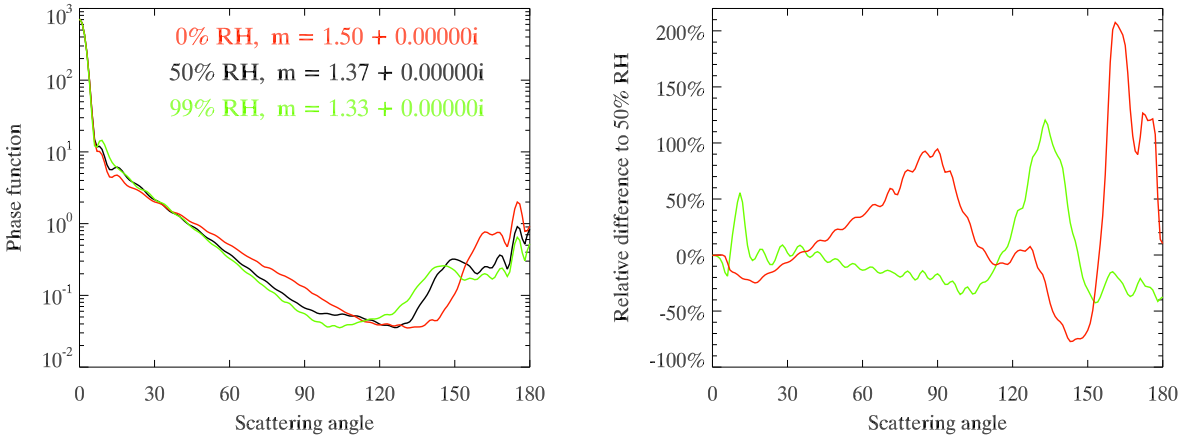

Figure 2.2: Phase function and relative differences in phase functions for three different types of salt from OPAC. All types have the same distribution of radii, but are in environments with differing refractive indices. In the second figure, the particles' with RH 0% and 99% are being compared to the 50% RH particles.

2.2 Mineral Dust

2.2.1 Background

A large body of work has concentrated on mineral dust aerosol, it being the most prevalent class in several areas of the world. Measured and assumed properties are summarised in the following tables.

Certain characteristics (introduced in §1.1) are used to generalise the classification of aerosol shape. Many campaigns have used images from scanning electron microscopy (SEM) and transmission electron microscopy (TEM), which provide 2D images. As such, it is almost always the projected features of a particle onto an image plane, that are analysed. Studies where the shape of the particle was not analyzed have not been included. Scattering methods employed in these studies include Mie theory, the discrete dipole approximation (DDA), T-Matrix theory and ray tracing.

Where an entry in the following table is left blank (i.e. " - " instead of text), it means that the column is not appropriate in this case. For example, Volten et al. [No date] in Table 2.1 refers to a database of light scattering properties which lists samples from all over the world. In this case the properties column is not appropriate as no conclusions as to particle shape are listed.

Table 2.1: Measurement of dust properties

Reference	Location	Method	Properties
Volten et al. [No date]	Dust from various worldwide locations.	Analysied using SEM and measurement of phase function.	-

Table 2.1 continued ...

Reference	Location	Method	Properties
[Buseck et al., 2000]	Asian dust	TEM analysis.	Mean AR ~ 1.5.
[Okada et al., 2001]	Three arid regions in China.	SEM analysis.	Mean AR $\sim 1.3 \rightarrow 1.6$. CIR decreased with increasing radius, suggesting aggregate particles at larger sizes.
[Haywood et al., 2003]	Sahara (SHADE experiment)	Measurements of dust by Met Office C-130 aircraft. Including Small Ice Detector (SID) and Passive Cavity Aerosol Spectrometer Probe (PCASP).	Asphericity factor (af) measured by SID is greater than 1, suggesting non-spherical scattering patterns when in the dust aerosol layer.
[Reid et al., 2003]	Puerto Rico (PRIDE experiment).	SEM analysis of airborne measurements.	Median $AR = 1.9$ with standard deviation 0.9 independant of size. Except, some of the largest particles ($> 10\mu$m, 13% of samples)are slightly elongated ($AR = 2.2 \pm 1.2$).
[Kalashnikova and Sokolik, 2004]	Representative Saharan and Asian dust samples.	SEM images analysed and circularity, non-sphericity and AR calculated. These are compared to values for known shapes.	Various shape distributions found. From these, models are created (see Table 2.2).
[Kandler et al., 2007]	Saharan mineral dust measured at Izaña, Tenerife.	Automated analysis of 22,000 particles from SEM images.	Above 1μm, the aerosol is dominated by mineral dust. Most particles have a coating of sulphates with average thickness 60nm. Formula for distribution of AR, $h(AR)$ provided (modified log normal). Average $AR = 1.64$. $RI = 1.59 + 0.007i$.

Table 2.1 continued ...

Reference	Location	Method	Properties
[Chou et al., 2008]	Niger, African Monsoon Multidisciplinary Analyses (AMMA)	FAAM flights, TEM and SEM. Aspect ratio (AR) calculated by comparing projected area to projected major axis from image for 790 particles.	AR is independant of size. Biomass burning particulate observed in fine fraction of mineral dust. Soot chains were not observed. "mineral dust particles could be described as ellipsoids" whose major axis never exceeds 2.2 times the minor axis.

Table 2.2: Modelling of dust properties

Reference	Method	Assumed properties	Conclusions
[Mishchenko et al., 1997]	T-matrix [Mishchenko and Travis, 1998].	"Equiprobable shape mixture of prolate and oblate spheroids" with AR ranging from $1.4 \rightarrow 2.2$ in steps of 0.2.	$P_{NS} \gg P_S$ for $90° \rightsquigarrow 150°$; $P_{NS} \ll P_S$ for $150° \rightsquigarrow 180°$, where P_S, P_{NS} are spherical and NS phase functions.
[Wang et al., 2003]	T-matrix [Mishchenko and Travis, 1998]	Composite phase fn $P(\theta) = \frac{1}{3}P_S + \frac{2}{3}P_{NS}$. The NS part is made up of spheroids with the same AR distribution as [Mishchenko et al., 1997].	Applying purely NS phase fns into satellite retrievals does not significantly improve them. Using both spherical and NS particles, a "great improvement" is found.
[Kalashnikova and Sokolik, 2004]	DDA and Mie. It would appear also T-matrix has been used (although not explicitly mentioned).	Four "representative" distributions containing in varying proportions spheres, spheroids, random shapes and hexagonal and rectangular disks. Spheroid distribution is as in Mishchenko et al. [1997].	**i)** Angular, sharp-edge particles cause largest differences in optical properties relative to spheres and spheroids increasing $\bar{\omega_0}$ and τ; **ii)** Effect of NS on $\bar{\omega_0}$ is more important for strong absorptive material; **iii)** "Because sharp-edge particles are often a major fraction [of total aerosol], NS effect cannot be ignored".

Table 2.2 continued ...

Reference	Method	Assumed properties	Conclusions
[Dubovik et al., 2006]	T-matrix [Mishchenko and Travis, 1998] & ray tracing [Yang and Liou, 1996] for larger particles.	There are no particles with AR < 1.44. The distribution of AR is a step function with n(AR) $= 0$ when $0.7 < \epsilon < 1.4$.	Stability of NS aerosol retrievals are increased if there is equal presence of prolate and oblate spherioids.
[Muñoz et al., 2007]	Ray tracing	"Realistic shapes" from the Amsterdam database [Volten et al., No date].	-
[Yang et al., 2007]	As Dubovik et al. [2006]. For large particles, surface roughness is also tested. TOA radiances calculated.	Assumed that all particles are spheroids with $AR = 1.7$ (both oblate and prolate). Also reviewed [Nakajima et al., 1989, Okada et al., 1987, Hill et al., 1984, Reid et al., 1993] finding that "mode or mean AR were 1.7, 1.4, ~ 2, 1.9 and 2.2".	"Non-sphericity effect of dust particles is significant at short wavelenghts, however, not at the thermal infrared".
[Hudson et al., 2008]	"Small particle regime"	Looked at needles, disks and continuous distributions of ellipsoids.	Disk simulations are the best fit for small clay particles.
[Mishra and Tripathi, 2008]	T-matrix [Mishchenko and Travis, 1998].	Used spheres, oblate spheroids with $AR = 1.5$ and Chebyshev particles.	"Effect of haematite variation on $\bar{\omega_0}$ is found to be stronger than particle nonsphericity".
[Osborne et al., 2008]	T-matrix [Mishchenko and Travis, 1998].	Oblate and prolate spheroids with $\epsilon = 1.7$ as "this was the median value found from SEM analysis".	-

From Table 2.2 we find that the most common method of modelling of mineral dust aerosol encountered was with Mishchenko and Travis' T-matrix code [Mishchenko and Travis, 1998]. Spheroids were the most common NS shape used, one of two tactics for describing the shape distribution being employed. Some works picked a single representative aspect ratio, generally with a value of $\sim$1.6

[Yang et al., 2007, Mishra and Tripathi, 2008, Osborne et al., 2008], while others used a distribution of aspect ratios with equal probability [Mishchenko et al., 1997, Wang et al., 2003, Kalashnikova and Sokolik, 2004, Dubovik et al., 2006]. Ray tracing was sometime used for the more randomly shaped particles, or where the T-matrix method was not possible [Haywood et al., 2003, Dubovik et al., 2006, Yang et al., 2007]. DDA was not generally used in studies of this sort[1], since it places an unfeasibly large strain on computing resources in most cases. All studies conclude that including NS components of aerosol in light scattering models improve the agreement of phase functions with those observed. Interestingly, Wang et al. [2003] noticed that using only NS aerosol did not give so good an improvement in satellite retrievals as a mixture of spherical and NS particles.

The measurement experiments which are of the most use in trying to look at particle shape are those using electron microscopy. The overall picture from Table 2.1 is of particles with rough edges and aspect ratios of $1.3 \rightarrow 2.2$. The AR distributions are generally reported to be independent of size, at least for all but the largest particles where Reid et al. [2003] found that particles with radius $> 10\mu$m were more elongated. In the case of Kandler et al. [2007], the distribution of aspect ratios, $n(AR)$ was assumed to be a modified lognormal function given by,

$$n(AR) = \frac{1}{\sqrt{2\pi}\sigma(AR-1)} \times \exp\left[-\frac{1}{2}\left(\frac{\ln(AR-1)-\mu}{\sigma}\right)^2\right], \tag{2.1}$$

with $\sigma = 0.6579$ and $\mu = -0.4502$ giving a median aspect ratio $AR = 1.65$. The fit to this curve is very convincing (see Fig. 10 from Kandler et al. [2007]).

The larger particles were generally said to be more "angular" or have "sharper edges" than those which were smaller [Haywood et al., 2003, Reid et al., 2003, Muñoz et al., 2007, Chou et al., 2008], although that is not to say that this requires the AR of a shape to change. Yang et al. [2007] used ray tracing to give larger particles a "rougher" surface. Their justification for this was from inspection of electron micrographs of dust particles[Reid et al., 2003]. Another option with larger particles is to consider them as "irregular aggregates" with rougher contours [Reid et al., 2003, Chou et al., 2008]. This has not been used to model mineral dust in any of the papers reviewed.

Some sources also commented that a thin coating of sulphate ($\sim$ 60nm) was found on samples [Kandler et al., 2007, Chou et al., 2008].

2.2.2 Optical calculations

As in the majority of previous strudies, the T-matrix method is used to calculate the light scattering from spheroid mineral dust particles.

Different distributions

Fig. 2.3 shows four possible aspect ratio distributions we can use to give our best description of aerosol properties in the atmosphere. Our current assumption of sphericity is the yellow distribution. We also looked at other distributions in AR space, as used in previous studies.

- Polydisperse with equal probablity of all ARs between 1.5 and 2.5.
- Monodisperse, with AR = 1.6.
- Polydisperse, with lognormal distribution, as given in [Kandler et al., 2007] and explicitly stated as (2.1).

[1] with the exception of Kalashnikova and Sokolik [2004]

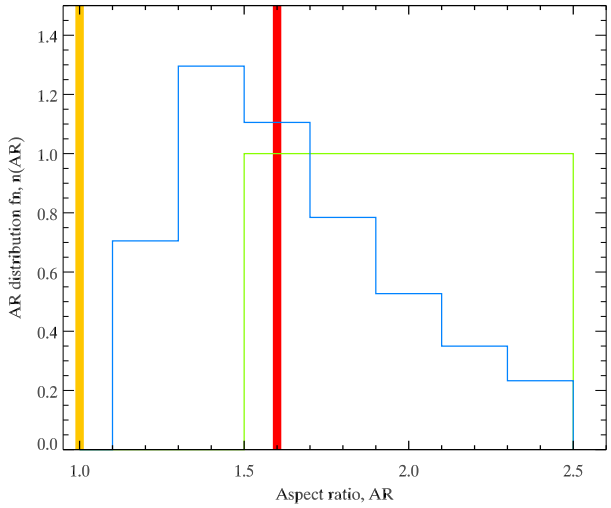

Figure 2.3: Various distributions of spheroid aspect ratios. Single lines imply a single value used, for example, yellow is a spherical distribution, which can be calculated using Mie theory. The blue distribution is a discretised version of (2.1), as used by Kandler et al. [2007]. The green distribution is a polydisperse distribution as used by Mishchenko et al. [1997].

Example phase functions for these aerosols, with lognormal size distributions are shown in Fig. 2.4. This case has a distribution effective radius of 2.26 μm (towards the larger end of mineral dust distributions). As usual, a lognormal distribution of sizes is used, and the only difference between the lines are the distributions of nonsphericity. The relative difference between the new, NS models and the spherical case are shown in the right hand plot. Initial impressions are that the phase function differences are very large in the back scatter, while manageble in the forward direction. Additionally, the differences from the spherical distribution are similar for the three NS distributions, that is, all three distributions alter the phase function in a similar way.

Taking the most physically justifiable distribution from Fig. 2.3, that of Kandler et al. [2007], we investigate the changes in phase function over a range of effective radii in Fig. 2.5. The main thing to say is that with increasing particle size, the differences between the NS and spherical distributions become more pronounced. Biggest differences occur at scattering angles between 100° and 150° and are always positive, agreeing with previous findings by Mishchenko et al. [1997]. For the larger particles, differences between the expected intensity at these angles can be as large as 200%. In the backscatter direction ($\theta > 150°$), negative differences occur, but generally, these are much less than the positive differences at slightly lesser scattering angles. For distributions with effective radii $< 1\mu$m, the mean relative difference in the phase function is less than 10%.

According to Dubovik et al. [2006], problems occured when *only* oblate, or *only* prolate spheroids were used. It was reported that "the assumption of an equal presence [...] resulted in improved stability of the retrievals". Comparing these individual functions to the full function, Fig. 2.6 shows how oblate only and prolate only functions differ by quite large amounts from their combined function. The errors shown are mirror images of each other, as the full function is an combination in equal parts of the two other functions. Errors of over 10% in the back scatter direction for these plots present a serious worry. It is in no way clear whether oblate or prolate spheroids (or a combination of the two) are the most effective representations for mineral dust. That using one or the other will affect scattering properties so greatly (although not as greatly as with spherical comparisons) leads to an arbitrary choice in this exercise.

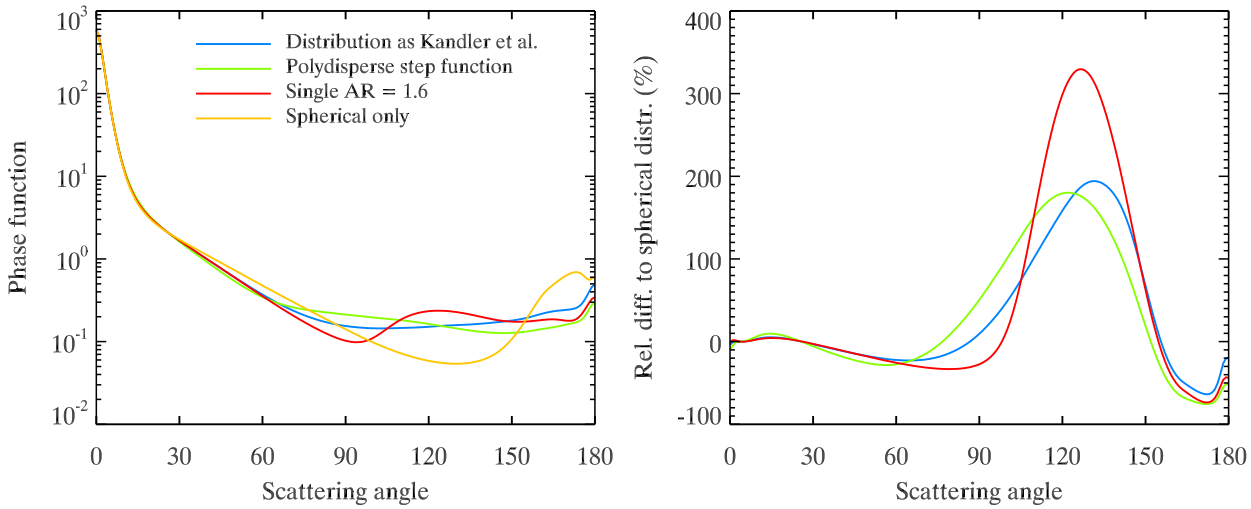

Figure 2.4: Phase functions for spheroid AR distributions (as given in Fig. 2.3) with a lognormal distribution of particles sizes. Relative difference between the spheroid distributions, and a spherical only distribution are shown in the right hand figure. Spheroid distributions use equal numbers of oblate and prolate spheroids.

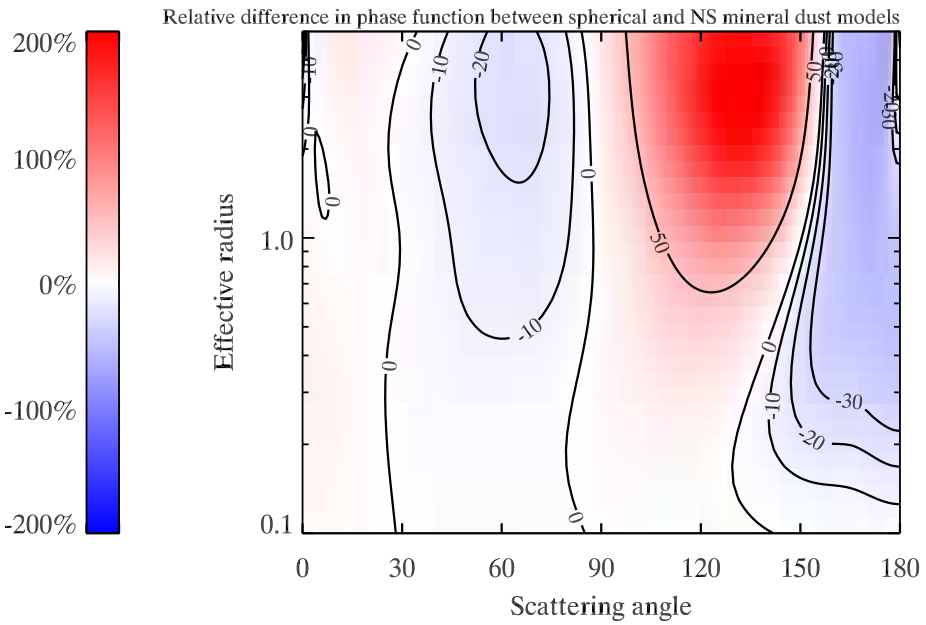

Figure 2.5: Relative difference between NS to spherical phase functions over a range of particle sizes. Distribution of NS particles is that of Kandler et al. [2007] as shown in Fig. 2.3.

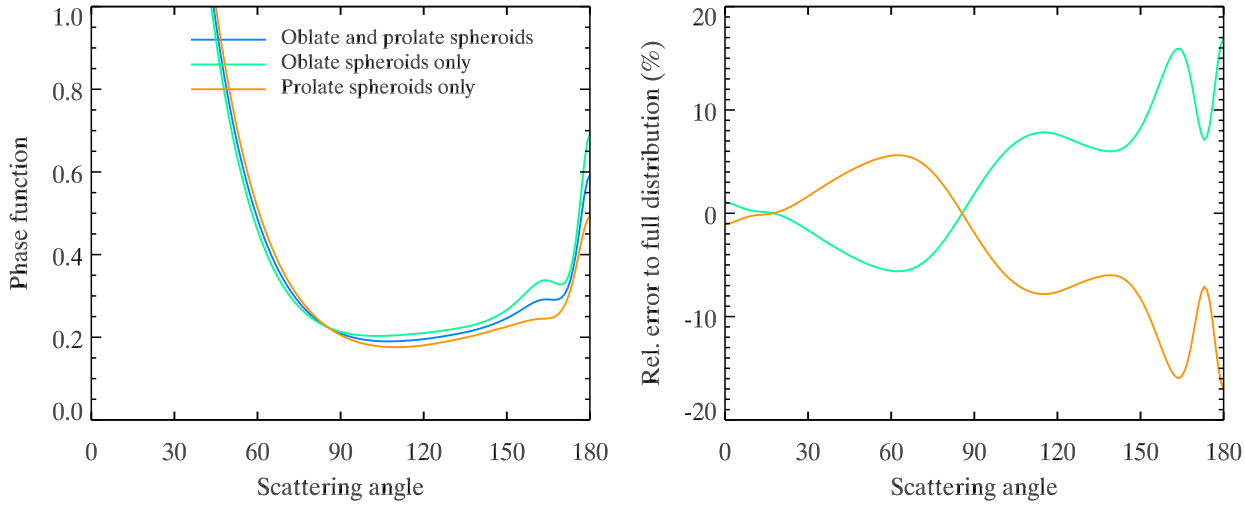

Figure 2.6: Phase functions for lognormal spheroid AR distributions. Relative differences between the spheroid distributions, and a spherical only distribution are shown in the right hand figure.

2.3 Black carbon

2.3.1 Background

Black carbon (BC) is a more problematic aerosol to model. It is formed by the combustion of carbon-rich organic fuels in conditions of insufficient oxygen supply. This can include biomass burning, internal combustion engines and aircraft engines. Reported absorption varies greatly, but it always significant (the imaginary part of BC's refractive index has been reported between 0.0093 and 0.1 [Hungershoefer et al., 2008]). Particulates produced are fractal like agglomerates of spherules, having great structural variability. Fig. 2.7 shows a typical TEM image of BC close to source in which one can clearly see the individual "blobs" that compose the aggregate whole.

BC does not stay as a chain for long. As time progresses, ageing and wetting processes cause the chains to collapse, giving them an almost spherical shape. BC ageing time scales of 2–8 hours in daytime are not unusual [Schnaiter et al., 2005]. Colbeck et al. [1990] looked at how humidity and clouds affect the morphology of the BC chains, for example, fig. 2.8 shows an example from this work, where cloud processing causes immediate curling up of chains as they cluster and take on a more spherical shape.

Additionally, as the the aerosol age in the atmosphere, they act as nucleation sites for water. Studies show that away from combustion sources, a large proportion of atmospheric BC is seen in internal mixtures with water solouble compounds, particularly sulphates[Hasegawa and Ohta, 2002, Schnaiter et al., 2005].

In summary, we are presented with a more complex problem when we consider biomass burning aerosol, its evolution and its interaction with aqueous species. At the same time, the evolution towards more spherical morphology as the aerosol ages should make scattering calculations much simpler for aged BC.

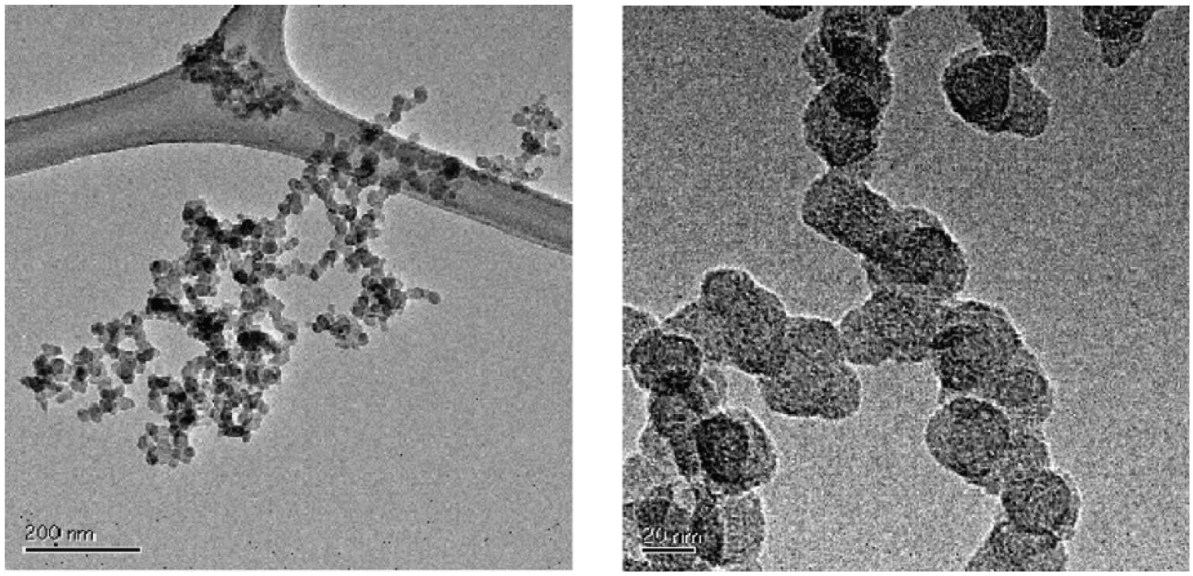

(a) (b)

Figure 2.7: TEM images of typical black carbon aggregates, soon after their creation. From Kirchstetter and Novakov [2007]

2.3.2 Optical calculations

As discussed in the previous section, an initial, simple improvement in the optical modelling of aged biomass burning aersol is to consider it as coated soot particles, layering water, or sulphate over the main particle. Fig. 2.9 shows a coated soot particle collected in Japan. In a study by Schnaiter et al. [2005], it was noted that using layered spheres to model the interal mixing of BC with secondary organic carbon (SOC) could accurately reproduce the amplification of the absorption cross section although other optical properties agreed less successfully with measurement. As such, the coating of biomass aerosol with liquid could be a sensible first step.

The aerosol's size is now a matter for debate. Is it the size before being coated with a second layer, or after? Since this project is looking from the point of view of final aerosol measurement from optical properties, the second approach is taken. We would never know what the particles original size is.

The new model of our aerosol scatterer is shown in Fig. 2.10. The aged biomass burning aerosol is given the properties presented in Dubovik et al. [2002] which provides measurements of biomass burning aerosol optical properties including the details of the lognormal distribution parameters.

We can choose to define the thickness of the outer, water layer in one of two ways: either as a fraction of the total thickness, or as a set thickness, independent of inner aerosol size.

In the 1st method, the total radius of our coated aerosol is R, of which the outer $x\%$ is a water coating. The inner, soot sphere has radius $r_s = R \times \left(1 - \frac{x}{100\%}\right)$ and complex refractive index m_s. The refractive index of water is m_w. The phase function can now be calculated for a variety of values of x.

In our second method, the total radius of our coated aerosol, $R = r_s + x$, where the thickness of the outer coating is x. In this case, we obviously can't include particles with radii smaller than $R_{\min} = x + \delta r_s$.

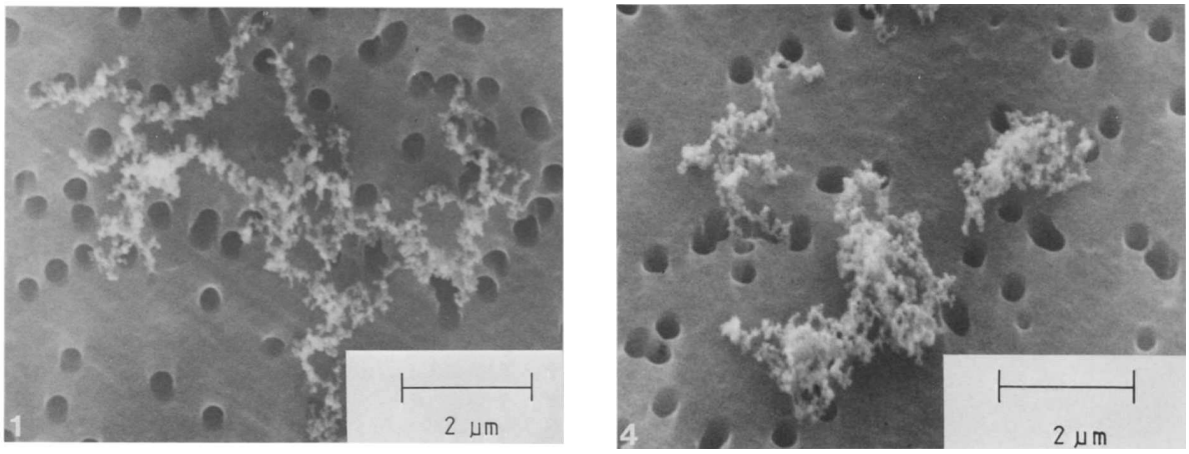

(a) Initial sample at 4hrs (b) After being subjected to 2.4% supersaturation

Figure 2.8: TEM images of smoke which has aged for 4hrs. Elemental carbon content was >95%. From Colbeck et al. [1990].

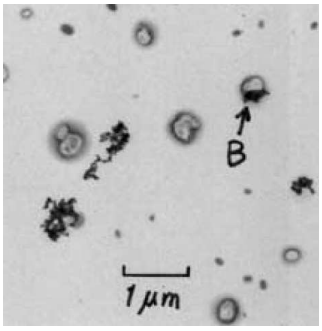

Figure 2.9: TEM image of particles collected by Hasegawa and Ohta [2002]. The particle marked (B) is an internal mixture containing soot.

Thickness by percentage

Fig. 2.11 shows phase functions of these new aerosol components. The spherical scatterers are replaced with a double layer arrangement with various amounts of water present in the aerosol. The size distribution (which is lognormal) is not altered. The curve with $x = 0\%$ is essentially a sphere with no water (Mie theory). Other values are compared to the spherical case which would have been our previous assumption. The first thought has to be that these different models, all with a spherical soot core, have values varying by as much as 500%. Working under the assumption that our layered representation is better (if only slightly) than our previous, spherical guess, this is not an insignificant difference.

The single scattering albedo is seen to increase as more water is added to the outside of our aerosol. This is perfectly reasonable, as we are replacing a non-absorbing medium in the place of an absorbing one. This can be clearly seen in Fig. 2.12 for both individual particle sizes and the whole size distribution. There appears to be a tipping point at around $x = 25\%$ beyond which, the SSA increases rapidly with increasing water. This can be compared with Abel et al. [2003] where the evolution of aerosol co-albedo ($= 1 - \bar{\omega_0}$) is measured downwind of biomass burning source, and is seen to become less absorbing over time, with $\bar{\omega_0}$ increasing.

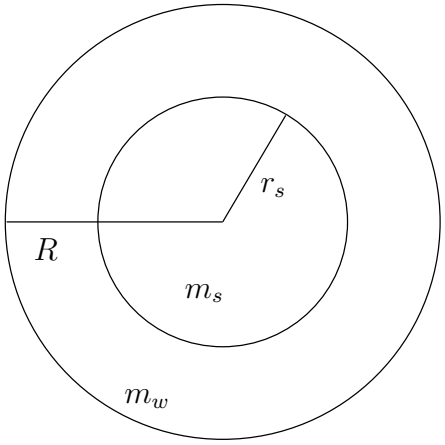

Figure 2.10: Showing a model for a coated sphere. The outer layer is water, with refractive index m_w and has a thickness $(R - r_s)$. The inner sphere, with refractive index m_s has radius r_s. The total radius of the aerosol is R.

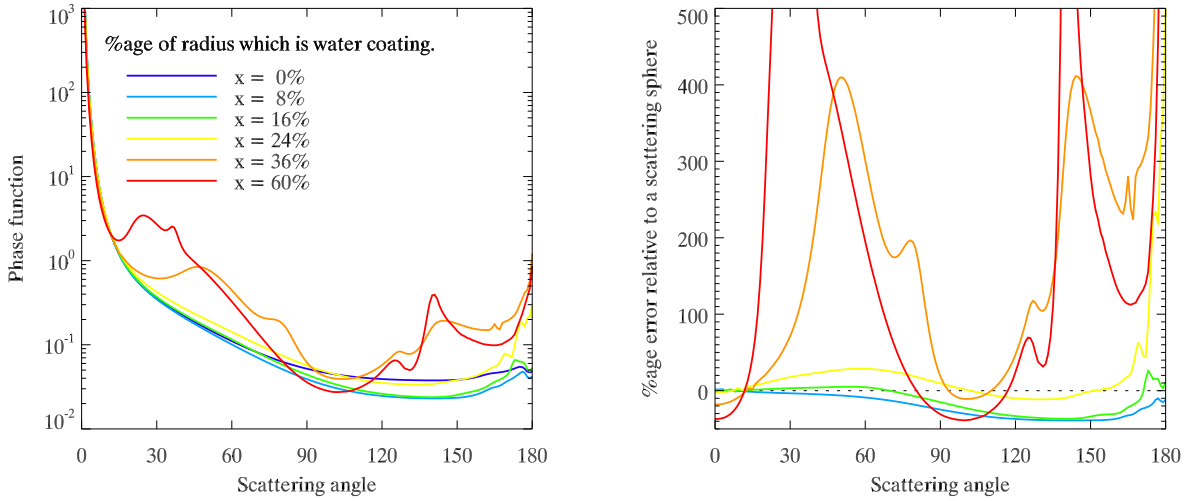

Figure 2.11: Modelling aged biomass burning aerosol for a lognormal size distribution. Biomass is defined as a sphere of soot, surrounded by a concentric sphere of water. The left hand plot shows phase functions for various aerosol distributions. The right hand plot shows the differences between the modified phase functions, and the original Mie theory. The thickness of the coating is defined as a percentage of the total aerosol thickness.

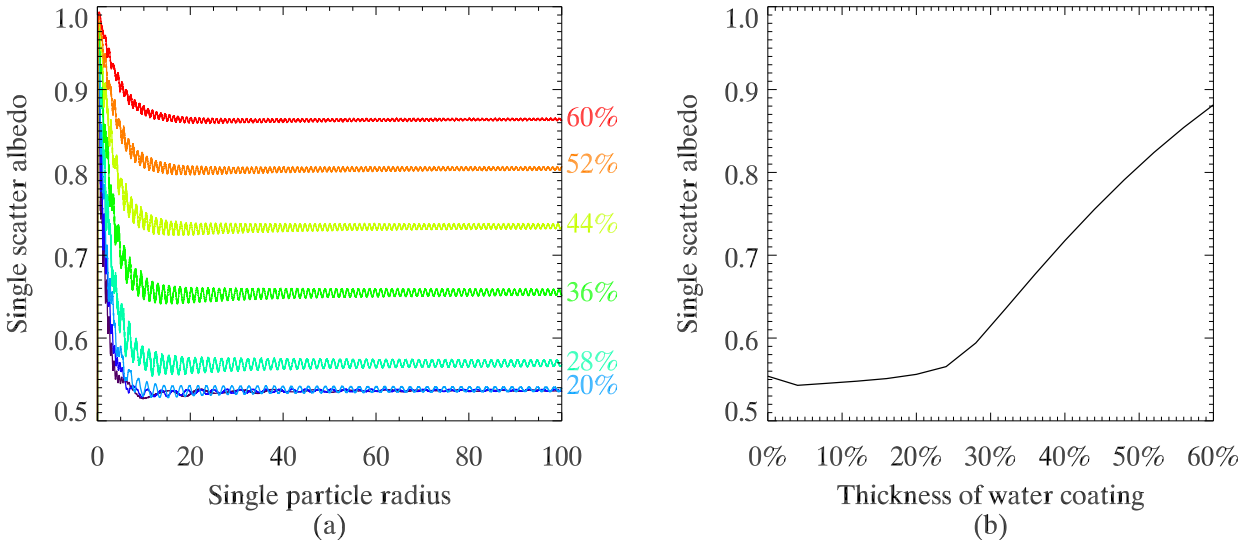

Figure 2.12: Single scattering albedo plots. (a) shows the variation of SSA with increasing particle radius for various values of water coating thickness, x. (b) shows the trend for a normally distributed sample as the thickness of the water coat increases.

Thickness as fixed value

Fig. 2.13 shows the phase functions for fixed coating thicknesses with each distribution of radii of biomass aerosol. It is immediately obvious that differences between this method the that of the previous section are large. This is to be expected. While fixed thickness will cause relatively thick coatings of water for smaller particles, fractional thickness leads to thick coatings of water for the larger particles. Since larger particles will have larger scattering cross-sections, the previous example is reasonably expected to differ more from the homogeneous, spherical scattering model.

Nevertheless, we see considerable differences in the back scatter values of the phase function for coatings of a few hundred nm. For the very thick coatings (e.g. 2 μm), differences are once again in the hundreds of percents. Interestingly, Fig. 2.13 shows that the coating which has the least difference from the homogeneous case is not the one with the thinest coat, but one with a thickness of 0.3 μm.

Fig. 2.14 shows the relative difference in phase function as a function of effective radius, for a selection of shell thicknesses. Unlike the mineral dust case, where relative differences increased with radius, in the coated case, differences are less predicable. This is expected, since the the large particles have the same thickness of coating as the small ones, and as such, one would expect large differences for the small particles. As in the mineral dust case, changing from a spherical, scattering model causes large differences of order 100% in the phase function.

As expected, single scatter albedo also increases with increased water content. The effect is far less pronounced now we are no longer looking at particles which have 10 times more water by volume than the carbon we are supposed to be looking at. Fig. 2.15 shows the change in SSA as a function of effective radius and thickness of water coating. Predictably, increases in the effective radius decrease the effect of a coating of fixed thickness, and increasing the thickness increases the SSA as more non-absorbing material is present in the scatterer.

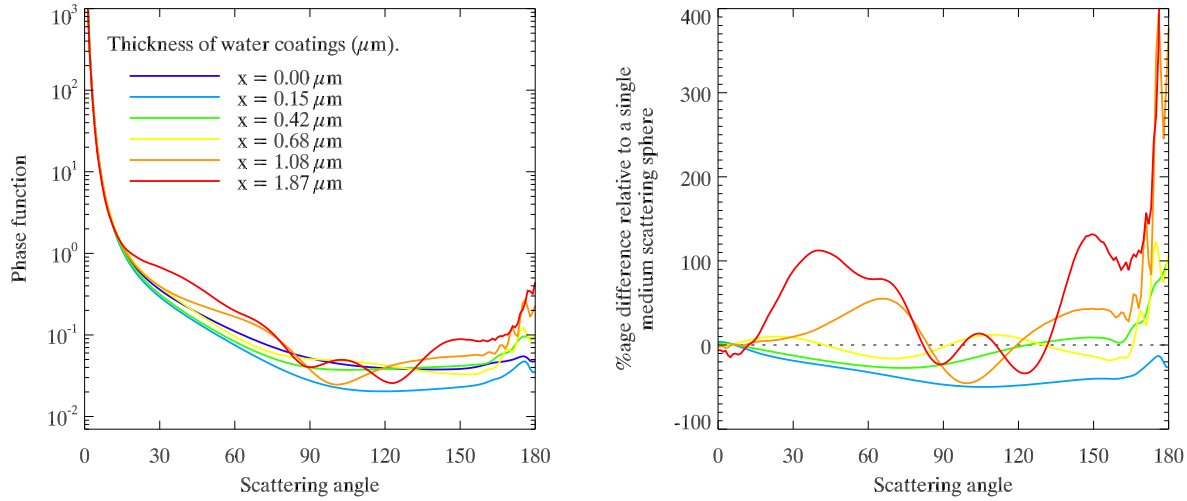

Figure 2.13: Modelling aged biomass burning aerosol for a lognormal size distribution. Biomass is defined as a sphere of soot, surrounded by a concentric sphere of water. The left hand plot shows phase functions for various aerosol distributions. The right hand plot shows the differences between the modified phase functions, and the original Mie theory. The thickness of the coating is fixed for all particles, regardless of size.

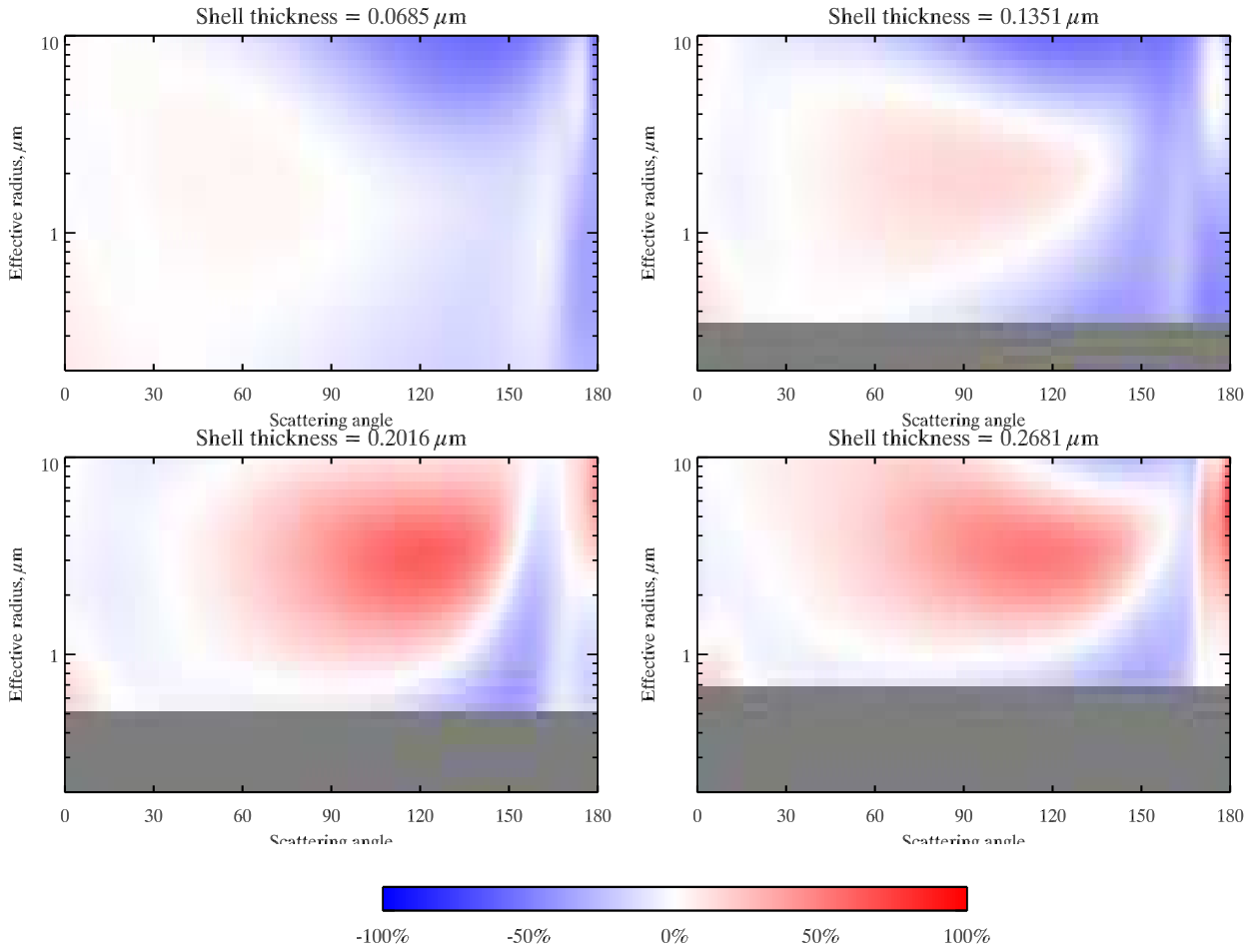

Figure 2.14: Relative difference in phase function compared to spherical case for four different coated sphere cases. Grey sections of the graph indicate areas where the shell thickness prohibits distributions with effective radii so small.

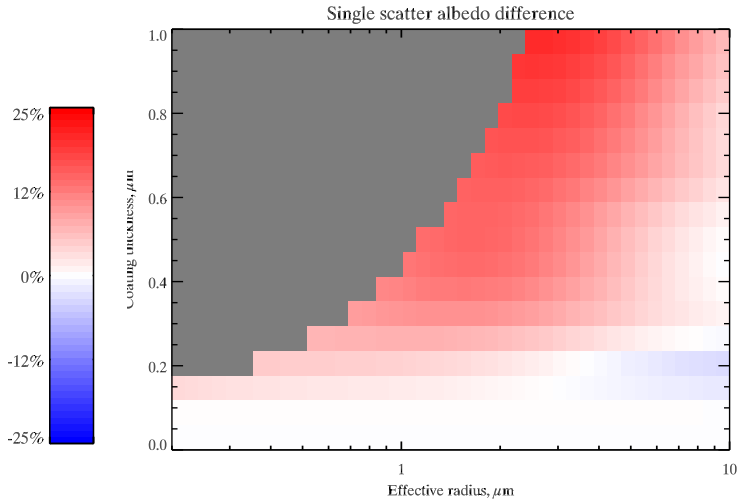

Figure 2.15: Single scatter albedo relative difference from spherical case as a function of effective radius and thickness of coating. The grey areas of the graph are where the thickness of the coating prohibits distributions with effective radii so small.

Chapter 3

Case study - Saharan Sand

Look up tables were created to go into ORAC retrievals over the Saharan area. Classes of aerosol are defined as a combination of several aerosol modes, each with their own refractive index, median radius and radius standard deviation. In the mineral dust class (which currently consists of four aerosol modes), the spherical coarse, accumulation and nucleation components of mineral dust in the aerosol tables were replaced with spheroid minerals as shown in the previous section. The final componet, a water soluble aerosol was left spherical. The effective radius of the classes are calculated by modifying the mixing ratios of each aerosol mode so that the total effective radius matches that required.

3.1 Scattering examples for the mineral dust class

Fig. 3.1 shows a comparison of phase functions between a new version of the mineral dust aerosol class, incorporating non-spherical components, and the standard, spherical aerosol only version. Additionally, since the DISORT radiative transfer model does not deal directly with phase functions, but instead, with Legendre coefficients[1]. Although this can lead to errors (if the series is terminated before high order terms are close enough to zero to make them negligable), results here show that errors are very small compared to the differences between spherical and NS aerosol classes. A mineral dust class effective radius of $r_{\text{eff}} = 1.624\,\mu$m is shown, being in the middle of expected range of $1 \rightarrow 2\,\mu$m [Hess et al., 1998].

As discussed previously, the change in aerosol shape has caused the phase function to increase in the backscatter direction, but decrease for scattering angles of $90° \rightarrow 150°$. In the infrared channel shown, differences are much less, since the size parameter for longer wavelengths is for the most part, less than unity[2]. Errors in the phase function peak at over 70% in this case, at scattering angles of around 120°. This is remarkably convenient for AATSR whose nadir view is generally in the range $110° \rightarrow 130°$. In the forward view, generally between $70° \rightarrow 90°$, errors are much smaller, suggesting that this view would be less suceptible to errors in retrievals due to spherical assumptions.

Impressively, although we see large changes in the phase functions between the two versions of mineral dust, the aerosol component, "Water Soluble, 50% humidity", which is spherical, actually accounts for 87% of the aerosol in the class at this radius. Additionally, of the sand components, over 50% of the next most populous mode (the nucleation mode, with 11% of aerosol) have a size parameter of less than 1. That leaves a very small proportion of particles (maybe 6%) which are

[1] Expansion coefficients for the phase function in terms of Legendre polynomials Arfken and Weber [1995].

[2] For $\lambda = 12.05\,\mu$m and $r_{\text{eff}} = 1.624\,\mu$m as in the current example, the effective size parameter is $x_{\text{eff}} = 0.84$.

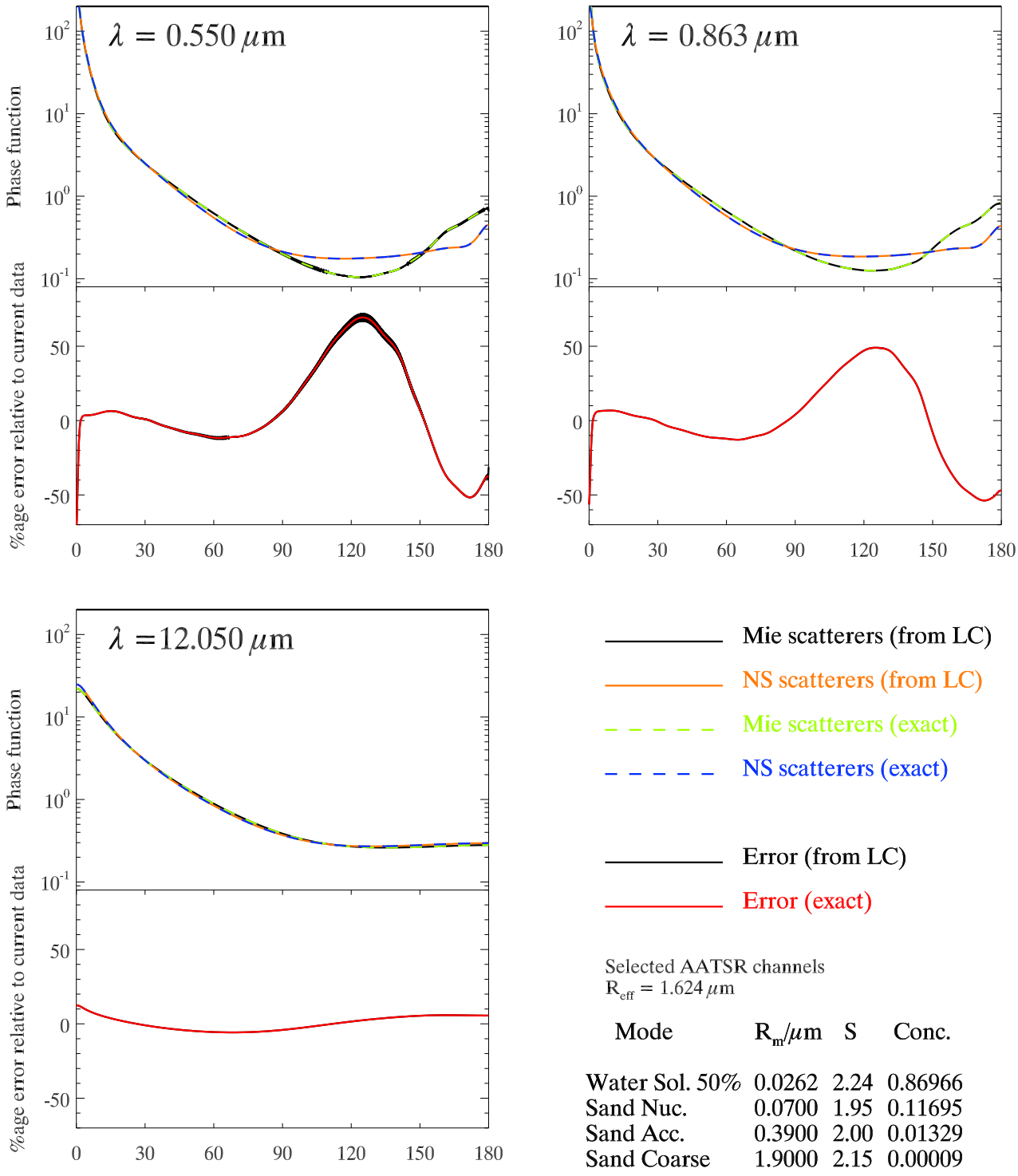

Figure 3.1: Mineral dust class phase functions for three selected AATSR channels. The effective radius in this case is $r_{\text{eff}} = 1.624\,\mu$m. NS and spherical models have been used and compared. In both cases, the refractive index, median radius (R_m), standard deviation of $\ln r$ (S), and external mixing ratios of each aerosol component are kept constant. The exact calculations, and those recalculated from a terminated series of Legendre coefficients are shown.

nonspherical, and are large enough to have phase functions which significantly deviate from the spherical case.

Looking at other effective radii (not shown), the trend is as might be expected. For small particles, the size parameters are smaller and when the wavelength of light becomes much greater than the radius, the shape of the scattering particle becomes unimportant, and errors relative to the spherical case decrease rapidly. Conversely, for larger particles, differences in shape become more pronounced, and errors relative to the spherical case increase accordingly. For the larger particles, the added problem that Legendre coefficients, terminated after 1000 terms (as is currently the case) fail to accurately reproduce the scattering patterns calculated increase errors. Since the inclusion of NS particles tends to blur the phase functions, making them less variable, this becomes less of a problem.

3.2 Top of atmosphere differences

After generating scattering properties for each aerosol class, the next stage is to put these properties into a forward model which gives top of atmosphere reflectance. Fig. 3.2 shows relative differences in reflectance between the non-spherical class (R_{A36}) and the spherical class (R_{A03}), as would be seen by AASTR.

The clearest difference is that for the smaller effective radii ($< 10\mu$m), there is very little difference between the two models. As particle size increases, the non-spherical particles are reflecting more light than their spherical counterparts with differences of 30% at very large effective radii. This is not the only option, however. Depending on the measuring angles of the satellite and the solar zenith angle, the changes can be largely positive or largely negative. The scattering angles selected in this case bare particular relevence to the nadir view for AATSR in the example retrieval given in the following section.

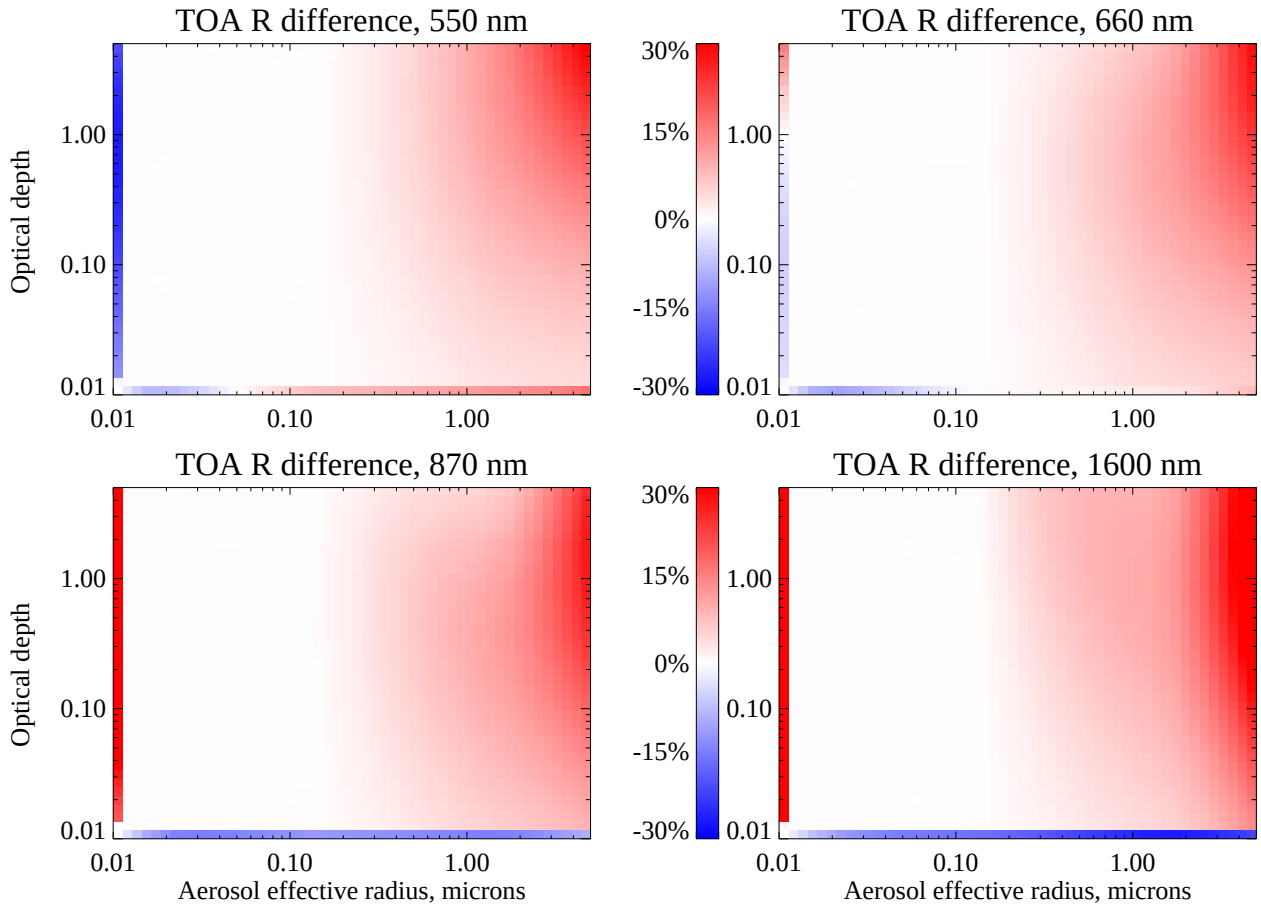

Figure 3.2: Showing relative differences in the top of atmosphere reflectance arriving at satellite from a Lambertion forward model for the spherical and non-spherical mineral dust aerosol classes. This example is for a solar zenith angle of 60°, satellite zenith angle of 55° and a relative azimuth angle of 15°. The difference is shown as a function of aerosol effective radius and aerosol optical depth. A positive difference implies that the non-spherical aerosol has greater reflectance

3.3 Retrieval differences

Fig. 3.3 shows the results of an AATSR retrieval off the West African coast from the 10th March, 2006. A large dust plume can clearly be seen in the centre of the image.

The retrieval has found that, in general, within the dust plume, the NS aerosol class provides a lower value of optical depth than the spherical aerosol. The effective radius is a less certain change, with some sections of the plume having larger and some smaller.

The cost difference[3] shows that within the plume, the NS class sometimes has the lower cost, while at other positions, the spherical class wins out. This suggests that the NS class is not significantly

[3]The cost of a retrieval gives a measure of how much the measurements differ from the predicted forward model values, and how much the state we are infering differs from the a priori information. In order to find our best estimate of a property, we minimise the cost function. The class is selected not only based on the class with minimum cost, but also, due to constraints on the radiance and optical depth for the mineral dust class. For example, even if a mineral dust class has the lowest cost, if the optical depth is less than 0.4, it will not be selected.

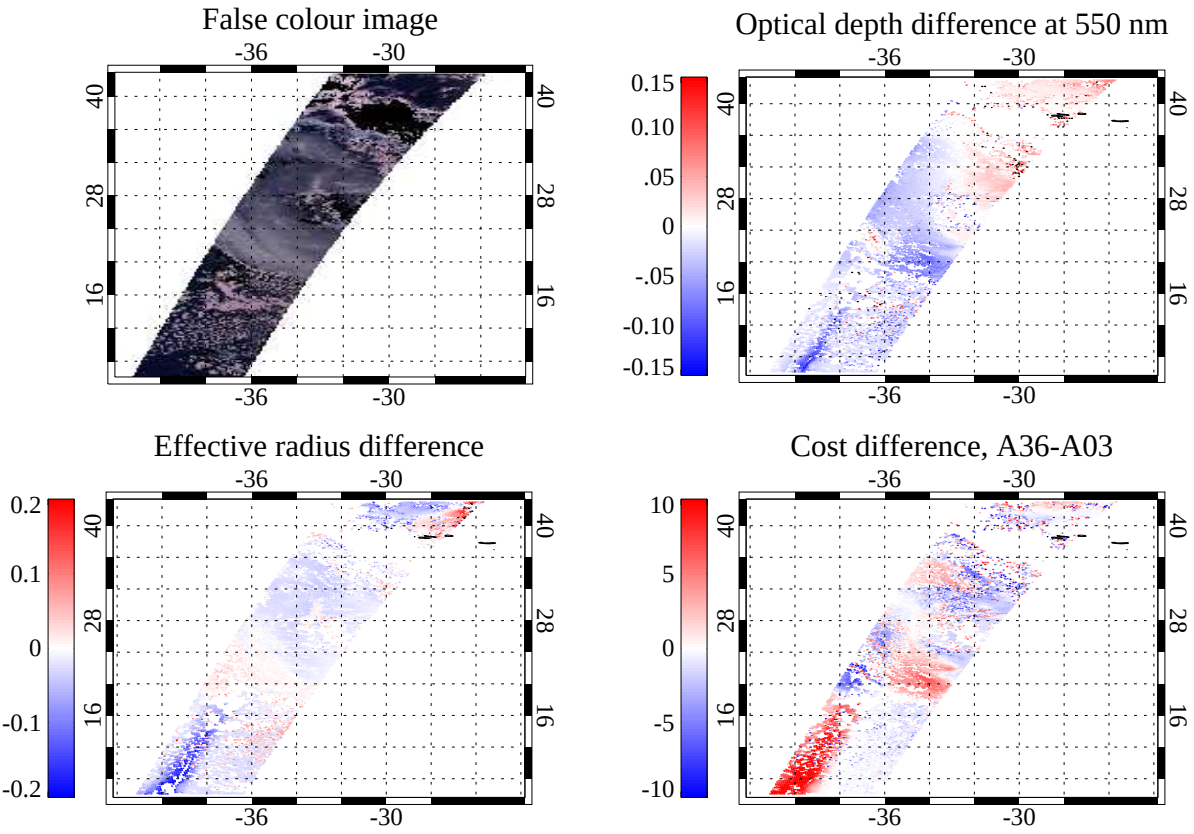

Figure 3.3: Properties from AATSR retrievals of aerosol from 10th March, 2006. Location is over the Atlantic, just off the West African coast. The islands to the top right are part of the Azores archipelago. The false colour image provides a representation of the scene from space. The difference in optical depth, effective radius and cost are then shown. In all cases, the spherical result is subtracted from the non-spherical result.

better at predicting the scattering from sand than the current spherical model. The clearest difference in cost occurs over the area south west of the plume, where cost for the NS class is much higher. This is encouraging, as it suggests that the NS class is less likely to confuse non-mineral dust aerosol for mineral dust.

While these results provide a first glance at altering the scattering model for a known NS aerosol in a retrieval, there is no way of knowing if they are representative without a more systematic study. Additionally, a particularly prominent dust storm was chosen as the first example. It would be of interest (although computationally expensive) to see how this new dust model alters the overall global statistics for optical depth and effective radius as well as cost.

Bibliography

Steven J. Abel, Jim M. Haywood, Eleanor J. Highwood, Jia Li, and Peter R. Buseck. Evolution of biomass burning aerosol properties from an agricultural fire in southern Africa. *Geophysical Research Letters*, 30(15):1783, 2003. doi: 10.1029/2003GL017342.

George B. Arfken and Hans J. Weber. *Mathematical Methods for Physicists*. Academic Press, 4th edition, 1995. Very good section on the associated Legendre polynomials (pp722–735). There is also a comprehensive guide to Bessel functions (pp627–692).

Craig F. Bohren and R. Huffman, Donald. *Absorption and Scattering of Light by Small Particles*. Wiley-VCH, 1983.

PR Buseck, DJ Jacob, M Posfai, J Li, and JR Anderson. Minerals in the air: An environmental perspective. *International Geology Review*, 42(7):577–593, July 2000. ISSN 0020-6814. Symposium Honoring the Contributions of Professor Konrad Krauskopf, Stanford, CA, December, 1999.

K. Chamaillard, C. Kleefeld, S.G. Jennings, D. Ceburnis, and C.D. O'Dowd. Light scattering properties of sea-salt aerosol particles inferred from modeling studies and ground-based measurements. *Journal of Quantitative Spectroscopy and Radiative Transfer*, 101(3):498–511, 2006. doi: 10.1016/j.jqsrt.2006.02.062. URL `http://www.sciencedirect.com/science/article/B6TVR-4JG46BT-B/2/62b2c95ea291dab05144b69ab33a974f`.

Cedric Chou, Paola Formenti, Michel Maille, Patrick Ausset, Guenter Helas, Mark Harrison, and Simon Osborne. Size distribution, shape, and composition of mineral dust aerosols collected during the African Monsoon Multidisciplinary Analysis Special Observation Period 0: Dust and Biomass-Burning Experiment field campaign in Niger, January 2006. *Journal of Geophysical Research - Atmospheres*, 113(D17), September 2008. ISSN 0148-0227. doi: 10.1029/2008JD009897.

I. Colbeck, editor. *Physical and Chemical Properties of Aerosols*. Blackie Academic & Professional, 1st edition, 1998.

I. Colbeck, L. Appleby, E.J. Hardman, and Roy M. Harrison. The optical properties and morphology of cloud-processed carbonaceous smoke. *Journal of Aerosol Science*, 21(4):527 – 538, 1990. ISSN 0021-8502. doi: 10.1016/0021-8502(90)90129-L. URL `http://www.sciencedirect.com/science/article/B6V6B-488G51G-10/2/53d5dc1bbdddc5b2deab13d824467d26`.

O Dubovik, B Holben, TF Eck, A Smirnov, YJ Kaufman, MD King, D Tanre, and I Slutsker. Variability of absorption and optical properties of key aerosol types observed in worldwide locations. *Journal of the Atmospheric Sciences*, 59(3):590–608, 2002. ISSN 0022-4928.

Oleg Dubovik, Alexander Sinyuk, Tatyana Lapyonok, Brent N. Holben, Michael Mishchenko, Ping Yang, Tom F. Eck, Hester Volten, Olga Munoz, Ben Veihelmann, Wim J. van der Zande, Jean-Francois Leon, Michael Sorokin, and Ilya Slutsker. Application of spheroid models to account for aerosol particle nonsphericity in remote sensing of desert dust. *Journal of Geophysical Research - Atmospheres*, 111(D11), June 2006. ISSN 0148-0227. doi: 10.1029/2005JD006619.

S. L. Gong, L. A. Barrie, and M. Lazare. Canadian aerosol module (CAM): A size-segregated simulation of atmospheric aerosol processes for climate and air quality models 2. global sea-salt aerosol and its budgets. *Journal of Geophysical Research - Atmospheres*, 107(D24):4779, December 2002. doi: 10.1029/2001JD002004.

Roy G. Grainger, Jonathan Lucas, Gareth E. Thomas, and Graham B. Ewen. Calculation of Mie derivatives. *Applied Optics*, 43(28):5386–5393, October 2004.

Shuichi Hasegawa and Sachio Ohta. Some measurements of the mixing state of soot-containing particles at urban and non-urban sites. *Atmospheric Environment*, 36(24):3899 – 3908, 2002. ISSN 1352-2310. doi: 10.1016/S1352-2310(02)00343-6. URL `http://www.sciencedirect.com/science/article/B6VH3-462BF3G-2/2/7f3a8f84df521a0e086f97380fdec327`.

J Haywood, P Francis, S Osborne, M Glew, N Loeb, E Highwood, D Tanre, G Myhre, P Formenti, and E Hirst. Radiative properties and direct radiative effect of Saharan dust measured by the C-130 aircraft during SHADE: 1. Solar spectrum. *Journal of Geophysical Research - Atmospheres*, 108(D18), July 2003. ISSN 0148-0227. doi: 10.1029/2002JD002687.

M. Hess, P. Koepke, and I. Schult. Optical properties of aerosols and clouds: The software package OPAC. *Bulletin of the American Meteorological Society*, 79(5):831–844, May 1998. ISSN 0003-0007. doi: 10.1175/1520-0477(1998)079⟨0831:OPOAAC⟩2.0.CO;2.

SC Hill, AC Hill, and PW Barber. Light-scattering by size shape distributions of soil particles and spheroids. *Applied Optics*, 23(7):1025–1031, 1984. ISSN 0003-6935.

Paula K. Hudson, Elizabeth R. Gibson, Mark A. Young, Paul D. Kleiber, and Vicki H. Grassian. Coupled infrared extinction and size distribution measurements for several clay components of mineral dust aerosol. *Journal of Geophysical Research - Atmospheres*, 113(D1), January 2008. ISSN 0148-0227. doi: 10.1029/2007JD008791.

K. Hungershoefer, K. Zeromskiene, Y. Iinuma, G. Helas, J. Trentmann, T. Trautmann, R. S. Parmar, A. Wiedensohler, M. O. Andreae, and O. Schmid. Modelling the optical properties of fresh biomass burning aerosol produced in a smoke chamber: results from the EFEU campaign. *Atmospheric Chemistry and Physics*, 8(13):3427–3439, 2008. ISSN 1680-7316.

N. Kaaden, A. Massling, A. Schladitz, T. Mller, K. Kandler, L. Schtz, B. Weinzierl, A. Petzold, M. Tesche, S. Leinert, C. Deutscher, M. Ebert, S. Weinbruch, and A. Wiedensohler. State of mixing, shape factor, number size distribution, and hygroscopic growth of the Saharan anthropogenic and mineral dust aerosol at Tinfou, Morocco. *Tellus B*, 61(1):51–63, 2008. doi: 10.1111/j.1600-0889.2008.00388.x.

OV Kalashnikova and IN Sokolik. Modeling the radiative properties of nonspherical soil-derived mineral aerosols. *Journal of Quantitative Spectroscopy & Radiative Transfer*, 87(2):137–166, August 2004. ISSN 0022-4073. doi: 10.1016/j.jqsrt.2003.12.026.

Konrad Kandler, Nathalie Benker, Ulrich Bundke, Emilio Cuevas, Martin Ebert, Peter Knippertz, Sergio Rodriguez, Lothar Schuetz, and Stephan Weinbruch. Chemical composition and complex refractive index of Saharan Mineral Dust at Izana, Tenerife (Spain) derived by electron microscopy. *Atmospheric Environment*, 41(37):8058–8074, December 2007. ISSN 1352-2310. doi: 10.1016/j.atmosenv.2007.06.047.

Thomas W. Kirchstetter and T. Novakov. Controlled generation of black carbon particles from a diffusion flame and applications in evaluating black carbon measurement methods. *Atmospheric Environment*, 41(9):1874 – 1888, 2007. ISSN 1352-2310. doi: 10.1016/j.atmosenv.2006.10.067. URL `http://www.sciencedirect.com/science/article/B6VH3-4MSHTKX-2/2/ccab7260cc0365510de052d8e65ad865`.

Peter Koepke and Michael Hess. Scattering functions of tropospheric aerosols: the effects of non-spherical particles. *Applied Optics*, 27(12):2422–2430, 1988. URL `http://ao.osa.org/abstract.cfm?URI=ao-27-12-2422`.

Ernie R. Lewis and Stephen E. Schwartz. *Sea Salt Aerosol Production: Mechanisms, Methods, Measurements, and Models—A Critical Review*, volume 152 of *Geophysical Monograph*. American Geophysical Union, 2000 Florida Avenue, N. W., Washington, DC 20009, 2004.

MI Mishchenko, LD Travis, RA Kahn, and RA West. Modeling phase functions for dustlike tropospheric aerosols using a shape mixture of randomly oriented polydisperse spheroids. *Journal of Geophysical Research - Atmospheres*, 102(D14):16831–16847, July 1997.

Michael I. Mishchenko and Larry D. Travis. Capabilities and limitations of a current FORTRAN implementation of the T-matrix method for randomly oriented, rotationally symmetric scatterers. *Journal of Quantitative Spectroscopy & Radiative Transfer*, 60(3):309–324, 1998. ISSN 0022-4073. 2nd International Workshop on Light Scattering by Non-spherical Particles, Helsinki, Finland, June 09-11, 1997.

Michael I. Mishchenko, Joop W. Hovenier, and Larry D. Travis, editors. *Light Scattering by Non-spherical Particles: Theory, Measurements, and Applications*. Academic Press, 2000.

S. K. Mishra and S. N. Tripathi. Modeling optical properties of mineral dust over the Indian Desert. *JGR*, 113(D23), December 2008. doi: 10.1029/2008JD010048.

O. Muñoz, H. Volten, J. W. Hovenier, T. Nousiainen, K. Muinonen, D. Guirado, F. Moreno, and L. B. F. M. Waters. Scattering matrix of large Saharan dust particles: Experiments and computations. *Journal of Geophysical Research - Atmospheres*, 112(D13), July 2007. ISSN 0148-0227. doi: 10.1029/2006JD008074.

T Nakajima, M Tanaka, M Yamano, M Shiobara, K Arao, and Y Nakanishi. Aerosol optical characteristics in the yellow sand events observed in May, 1982 at Nagasaki .2. models. *Journal of the Meteorological Society of Japan*, 67(2):279–291, April 1989. ISSN 0026-1165.

K Okada, A Kobayashi, Y Iwasaka, H Naruse, T Tanaka, and O Nemoto. Features of individual Asian dust-storm particles collected at Nagoya, Japan. *Journal of the Meteorological Society of Japan*, 65(3):515–521, June 1987. ISSN 0026-1165.

K Okada, J Heintzenberg, KJ Kai, and Y Qin. Shape of atmospheric mineral particles collected in three Chinese arid-regions. *Geophysical Research Letters*, 28(16):3123–3126, August 2001. ISSN 0094-8276.

S. R. Osborne, B. T. Johnson, J. M. Haywood, A. J. Baran, M. A. J. Harrison, and C. L. McConnell. Physical and optical properties of mineral dust aerosol during the Dust and Biomass-burning Experiment. *Journal of Geophysical Research - Atmospheres*, 113, July 25 2008. ISSN 0148-0227. doi: 10.1029/2007JD009551.

Reid et al., 1993. Likely to be typo in Yang et al. [2007] probably intending to cite Reid et al. 2003 [Reid et al., 2003].

EA Reid, JS Reid, MM Meier, MR Dunlap, SS Cliff, A Broumas, K Perry, and H Maring. Characterization of African dust transported to Puerto Rico by individual particle and size segregated bulk analysis. *Journal of Geophysical Research - Atmospheres*, 108(D19), July 12 2003. ISSN 0148-0227. doi: 10.1029/2002JD002935.

M. Schnaiter, C. Linke, O. M ohler, K.-H. Naumann, H. Saathoff, R. Wagner, U. Schurath, and B. Wehner. Absorption amplification of black carbon internally mixed with secondary organic aerosol. *Journal of Geophysical Research - Atmospheres*, 110:D19204, October 2005. ISSN 0148-0227. doi: 10.1029/2005JD006046.

C. M. Sorensen. Light scattering by fractal aggregates: A review. *Aerosol Science and Technology*, 35(2):648–687, August 2001. URL `http://www.informaworld.com/10.1080/02786820117868`.

H. C. van de Hulst. *Light Scattering by Small Particles*. John Wiley & Sons, 1957.

Hester Volten, Olga Muñoz, Joop Hovenier, and Rens Waters. The Amsterdam Light Scattering Database, No date. URL `http://www.astro.uva.nl/scatter/`.

J Wang, X Liu, SA Christopher, JS Reid, E Reid, and H Maring. The effects of non-sphericity on geostationary satellite retrievals of dust aerosols. *Geophysical Research Letters*, 30(24), December 30 2003. ISSN 0094-8276. doi: 10.1029/2003GL018697.

M. Wentzel, H. Gorzawski, K. H. Naumann, H. Saathoff, and S. Weinbruch. Transmission electron microscopical and aerosol dynamical characterization of soot aerosols. *Journal of Aerosol Science*, 34(10):1347 – 1370, 2003. ISSN 0021-8502. doi: 10.1016/S0021-8502(03)00360-4. URL `http://www.sciencedirect.com/science/article/B6V6B-498TSCY-4/2/ba30b8250a42627940ef023ddc6cbc33`. Intercomparison of Soot Measurement Techniques.

Yu-lin Xu and Bo Å. S. Gustafson. An analytical solution to electromagnetic multisphere-scattering — the scatterign formulation used in codes gmm01f.f and gmm01s.f. Technical report, Department of Astronomy, University of Florida, Gainesville, P.O. Box 112055, FL 32611-2055, No date.

P Yang and KN Liou. Geometric-optics-integral-equation method for light scattering by nonspherical ice crystals. *Applied Optics*, 35(33):6568–6584, November 20 1996. ISSN 0003-6935.

Ping Yang, Qian Feng, Gang Hong, George W. Kattawar, Warren J. Wiscombe, Michael I. Mishchenko, Oleg Dubovik, Istvan Laszlo, and Irina N. Sokolik. Modeling of the scattering and radiative properties of nonspherical dust-like aerosols. *Journal Of Aerosol Science*, 38(10):995–1014, October 2007. ISSN 0021-8502. doi: 10.1016/j.jacrosci.2007.07.001.